

Nanoscale Advances

Accepted Manuscript

This article can be cited before page numbers have been issued, to do this please use: K. Z. Ferdwushee, M. A. S. Chowdhury and S. T. Islam, *Nanoscale Adv.*, 2026, DOI: 10.1039/D5NA01063B.



This is an Accepted Manuscript, which has been through the Royal Society of Chemistry peer review process and has been accepted for publication.

Accepted Manuscripts are published online shortly after acceptance, before technical editing, formatting and proof reading. Using this free service, authors can make their results available to the community, in citable form, before we publish the edited article. We will replace this Accepted Manuscript with the edited and formatted Advance Article as soon as it is available.

You can find more information about Accepted Manuscripts in the [Information for Authors](#).

Please note that technical editing may introduce minor changes to the text and/or graphics, which may alter content. The journal's standard [Terms & Conditions](#) and the [Ethical guidelines](#) still apply. In no event shall the Royal Society of Chemistry be held responsible for any errors or omissions in this Accepted Manuscript or any consequences arising from the use of any information it contains.

Performance Improvement of an Au and TiO₂ Coated D-shaped Photonic Crystal Fiber (PCF) Based SPR Sensor for Cancer Detection

Kazi Zannatul Ferdushee, Md Abu Shahid Chowdhury*, Siddika Tamanna Islam

Department of Biomedical Engineering, Khulna University of Engineering & Technology,
Khulna 9203, Bangladesh

Corresponding author's email: shahid@bme.kuet.ac.bd

Abstract. Surface plasmon resonance (SPR) has been an emerging tool for the recognition of cancer in a label-free manner. However, conventional SPR setups are based on prism coupling, which makes them bulky, hindering their capability to be integrated into compact and portable devices. To overcome these issues, the proposed approach introduces a photonic crystal fiber (PCF) structure with a micro-channel D-shaped, integrated with a gold (Au) coating as the plasmonic substance and titanium dioxide (TiO₂) as a dielectric substance. It minimizes the distance of the plasmonic film from the fiber core, thus elevating the sensor performance. In addition, the introduction of TiO₂ over the plasmonic film alters the plasmon-analyte interaction, thus increasing the sensitivity. The numerical simulation for the designed sensor is done in COMSOL Multiphysics software through the finite element method (FEM). After optimization, the sensor is numerically evaluated for the identification of six various carcinoma cell types for refractive indices between 1.360 to 1.401. The ultimate achieved amplitude and spectral sensitivities are 717.29 RIU⁻¹ and 7142.86 nm/RIU, respectively, recorded for MCF-7 and MDA-MB-231 cells. Additionally, the optimized sensor can distinguish a diverse array of biomolecules across the RI span of 1.330 to 1.420, attaining a peak spectral sensitivity of 20,000 nm/RIU for y-polarized light. Moving further, the sensor also delineated excellent figure of merit, resolution, and amplitude sensitivity values of 366 RIU⁻¹, 5×10⁻⁶ RIU, and 1178 RIU⁻¹, respectively, within the mentioned RI domain. The measured outcomes show that the designed sensor could be a potential option for the precise identification of various cancer cells.

Keywords. Cancer, finite element method (FEM), Photonic crystal fiber (PCF), refractive index (RI), surface plasmon resonance (SPR)



31 1. Introduction

32 A total number of 618,120 cancer fatalities and 2,041,910 newly discovered carcinoma
33 cases are estimated to occur in the USA by the end of 2025 [1], [2], [3], [4]. The global death toll
34 projection is going up to 16.9 million per year by the year 2045. A significant portion of cancers
35 exhibit no symptoms until later stages, demonstrating the disease's complex and challenging
36 nature, with 70 % of cancer fatalities in resource-limited areas resulting from restricted access to
37 early screening and treatment [5]. Despite significant advances in conventional cancer detection
38 methods, such as imaging modalities like mammography, MR imaging, computed tomography
39 (CT), positron emission tomography (PET), and biopsies, as well as blood and tissue-based
40 diagnostic evaluation tools like polymerase chain reaction (PCR) and enzyme-linked
41 immunosorbent assay (ELISA), these mechanisms still endure major drawbacks. These include
42 low specificity, high costs, radiation exposure risk, time-intensive procedures, and dependency on
43 advanced laboratory setup, among others [6]. While AI and machine learning have contributed to
44 improved scan accuracy, these technologies still do not provide the kind of non-invasive, real-
45 time, and universal cancer detection needed [7]. Taking into consideration the significant
46 constraints that the traditional methods present, it is logical to say that the healthcare system needs
47 quick, inexpensive, and non-invasive diagnostic alternatives. A biosensor could be a probable
48 solution for overcoming the aforementioned limitations due to sensitive, selective, and time-
49 efficient analysis of biological targets in a user-friendly manner. Present-day biosensors use
50 enzymes and antibodies as biorecognition elements in their detection of cancer biomarkers [8], [9].
51 However, the use of enzymes and antibodies results in degradation over time, and subsequently,
52 the sensor performance is affected.

53 In this context, optical biosensors can hold significant potential in cancer diagnosis owing
54 to their real-time and continuous detection in a highly responsive, selective, and affordable, and
55 non-invasive manner. Different optical biosensors also have dependence on labeled techniques,
56 which incorporate electrochemically active probes, fluorescent labeling, and chemiluminescence.
57 Nevertheless, this method can be quite expensive, require a lot of time, and may also disrupt the
58 receptor-analyte interactions [10]. To avoid this problem, label-free optical sensors are strongly
59 recommended. Surface plasmon resonance (SPR) biosensors that allow the identification of target
60 substances at very low concentrations without the need for labeling are the most precise optical



61 methods [11], [12]. The SPR serves as a powerful tool for point-of-care testing of oncogenic
62 biomarkers in a label-free manner with high specificity, sensitivity, fast sensing, and high
63 repeatability, which can also characterize distinct types of carcinomas. The principle behind the
64 SPR biosensor is a shift in the refractive index (RI) in the ambient environment being measured
65 as it relates to the binding of molecules at the surface of the metal. A heterostructured SPR
66 biosensor composed of graphene and MXene ($Ti_3C_2T_x$), along with a BK7 prism, gold (Au), and
67 aluminum oxide (Al_2O_3) for the rapid characterization of a well-known cancer-associated marker,
68 carcinoembryonic antigen, was proposed by Khodaie and Heidarzadeh [13]. The findings
69 presented a figure of merit (FOM) of 17.52 RIU^{-1} and a comparatively enhanced sensitivity of
70 163.63 deg/RIU . The use of ZnO and TMDCs layers in a SPR biosensor by Janze et al. [11]
71 allowed for the identification of distinct carcinoma cells. The proposed biosensor demonstrated
72 the figure of merit and the highest sensitivity values of 124.86 RIU^{-1} and 342.14 deg/RIU in terms
73 of detecting blood cancer (Jurkat) cells from healthy cells. Another recent study proposed a $BaTiO_3$
74 and black phosphorus-based SPR biosensor for the identification of different malignancy
75 biomarkers, where a maximum sensitivity of 417.86 deg/RIU was achieved for breast cancer MCF-
76 7 cells (mammary carcinoma type II) [5]. On the other hand, the regular prism-coupled SPR setups,
77 which are the basis for sensing technologies, have some drawbacks, such as their large size, high
78 price, and the fact that they are difficult to incorporate into small, portable devices.

79 In this context, the fiber optic SPR sensors, particularly those utilizing Photonic Crystal
80 Fiber (PCF), so to speak, are the ones bringing the solution to the problems because they are
81 providing miniaturized, flexible, and robust platforms that are, at the same time compatible with
82 in vivo applications and point-of-care diagnostics [14]. These enticing features make PCF-based
83 SPR sensors desirable for various biosensing applications, including the detection of blood
84 components [15], heavy metals [16], cancer cells [17], and various other diseases [18].
85 Additionally, the use of AI for geometrical optimization has further enhanced the potential of PCF-
86 based SPR sensors for biomedical applications [19]. Among various fiber geometries, including
87 circular, D-shaped, slotted, and bowl-shaped, the D-shaped structure can improve sensor
88 performance by incorporating microchannels [20], [21]. Numerous researchers have reported a
89 wide variety of D-shaped structures for detecting various analytes. For instance, Divya *et al.* [22]
90 suggested a dual-channel D-shaped PCF-based plasmonic sensor that is able to sense two different



91 analytes simultaneously. The sensor went through an optimization process and then reached the
92 peak amplitude and wavelength sensitivities of 216 RIU⁻¹ and 10000 nm/RIU, respectively.
93 Another research work reported by Zhou *et al.* [23] was on a D-shaped PCF-based SPR sensor
94 whose core was an open-ring channel sandwiched between a gold deposition to trigger the
95 plasmonic modes. They showed that analyte placement significantly affects sensitivity.
96 Specifically, when the target analyte was positioned across the outer ring structure, the sensor
97 exhibited an RI finding that lies within the span of 1.2 to 1.34, achieving a peak sensitivity of 2000
98 nm/RIU. In contrast, when the analyte was placed only on the open channel, the measurable RI
99 span extended from 1.33 to 1.46, and the sensor achieved a peak sensitivity of 5600 nm/RIU. To
100 further improve the performance, Oudenani and Sonne proposed a D-Shaped SPR-Based PCF
101 biosensor, which obtained an optimum amplitude and wavelength sensitivity values of 1623.6
102 RIU⁻¹ and 12,300 nm/RIU, respectively [24]. On the other hand, Azadi *et al.* sandwiched a titanium
103 dioxide (TiO₂) dielectric material between the gold (Au) and the silica for light trapping. The
104 structure they suggested achieved an optimized wavelength sensitivity (WS) of 14,000 nm/RIU
105 and amplitude sensitivity (AS) of 610 RIU⁻¹. Moving further, Azadi *et al.* [25] conducted a study
106 wherein a TiO₂ dielectric coating was incorporated between a gold plasmonic layer and silica.
107 This structure achieved an optimized AS of 610 RIU⁻¹ and WS of 14,000 nm/RIU. Moreover, the
108 D-shaped design is efficacious in terms of production as it does not require a complicated setup,
109 as in the case of circular or dual-core PCF, besides being more durable with the Au or TiO₂
110 coatings, and allowing dual-polarization for further deterring of non-target interfering molecules
111 with [13] increased specificity.

112 Such facts have prompted this study to go for a D-shaped sensor, which facilitates enhanced
113 performance in distinguishing between different cancer cells and their normal counterparts. The
114 FEM is used to develop and investigate the designed sensor. The study critically examined how
115 the orientation of air spaces, their diameter, and the height of the plasmonic film and overlayers
116 affected the overall effectiveness of the sensor. The influence of the open channel on sensor
117 efficacy is also evaluated. After a thorough study and evaluation, it is concluded that the adjusted
118 sensor structure can identify six different cancer biomarkers from the corresponding healthy cells
119 with maximum amplitude and spectral sensitivities of 717.29 RIU⁻¹ and 7142.86 nm/RIU,
120 respectively, for MCF-7 and MDA-MB-231 cells. In addition, the optimized sensor exhibited a



121 maximum sensitivity, figure of merit, and resolution values of 20,000 nm/RIU, 1178 RIU⁻¹, 366
122 RIU⁻¹, and 5×10⁻⁶ RIU, respectively, within a wide RI span from 1.330 to 1.420 for y-polarized
123 light. This depicts the sensor's effectiveness in detecting a broad spectrum of bioanalytes with
124 enhanced performance, illustrating its potential to be a strong tool for medical diagnostics.

125 2. Design of PCF Structure and Theoretical Model

126 2.1. Overview of the PCF framework

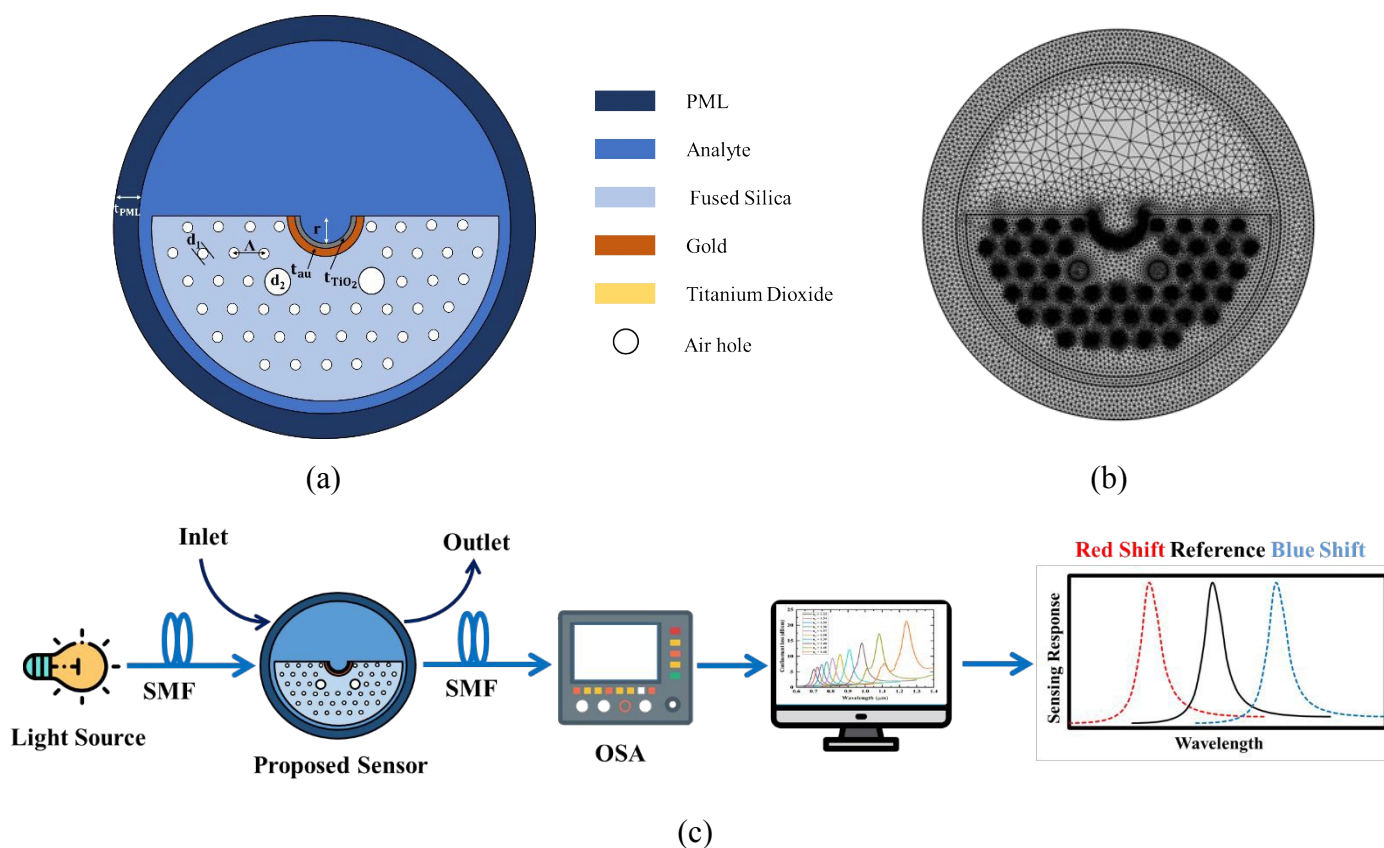
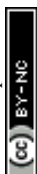


Fig. 1. Cross-sectional view of the (a) designed microchannel-type D-shaped sensor, (b) finite element mesh, and (c) experimental setup of the proposed sensor.

127 This study describes the design and numerical assessment of a SPR sensor based on PCF,
128 utilizing the full-vector FEM in COMSOL Multiphysics 6.1. Fig. 1(a-b) depicts the schematics of
129 the designed structure and finite element mesh. Simulations were conducted using a frequency-
130 domain eigenmode solver with a non-uniform triangular mesh. A non-uniform triangular mesh
131 with local refinement at the Au and Au-TiO₂ interface (192,032 domain, 6,136 boundary elements)



132 ensured convergence. Electromagnetic boundary conditions included PML at domain edges, and
133 continuity at material interfaces was implemented. Effective index and confinement loss were
134 extracted from $\text{Im}(n_{\text{eff}})$ using default solver tolerances. The sensor comprises three main
135 components: a silica (SiO_2) substrate featuring circular air spaces organized in a hexagonal lattice,
136 a gold (Au) plasmonic layer, and an analyte channel. The cladding region comprises two separate
137 types of air holes, labeled d_1 and d_2 , meticulously designed for superior optical confinement and
138 improved sensing efficacy. The midpoint-to-midpoint gap between neighboring air holes is labeled
139 as pitch, which determines the modal properties and the guided mode's effective refractive index.
140 A thin coating of TiO_2 is embedded between the Au layer and the analyte with a height of t_{TiO_2} .
141 After conducting a series of optimization experiments, the structural parameters have been
142 established as pitch = 4 μm , $r = 8 \mu\text{m}$, $d_1 = 1.1 \mu\text{m}$, $d_2 = 3 \mu\text{m}$, $t_{\text{Au}} = 55 \text{ nm}$, and $t_{\text{TiO}_2} = 09 \text{ nm}$. t_{Au}
143 indicates the height of the Au. The D-shaped arrangement is attained by polishing the fiber surface
144 near the core region, which minimizes the separation between the guided core mode and the Au
145 plasmonic layer. This reduced distance enhances the penetration of the evanescent electric field
146 into the plasmonic coating interface, increasing the modal overlap and improving phase matching
147 with the SPP mode, thereby strengthening SPR excitation and excitation efficiency. The external
148 section of the structure includes an analyte open microchannel with diameter r and a perfectly
149 matched layer (PML) with a thickness of $t_{\text{PML}} = 5 \mu\text{m}$, to mitigate undesirable boundary
150 reflections.

151 Fig. 1(c) explains a simplified representation of the experimental setting for the sensing
152 approach, including an optical tunable source (OTS) and an optical spectrum analyzer (OSA). The
153 designed sensor is interconnected via a single-mode fiber (SMF). The analyte is placed on the
154 external surface of the sensor, which can be regulated using a pump that passes through the
155 IN/OUT channel. The interaction between the unknown analyte and the sensor surface produces a
156 resonance wavelength shift toward the red or a blue shift, as depicted in Fig. 1 (c). The OSA can
157 monitor this phenomenon. The unidentified analyte can be determined by investing the
158 confinement loss on a computer.

159 **2.2. Material selection and theoretical basis**



160 Gold (Au) is an effective plasmonic substance due to its remarkable chemical stability,
161 biocompatibility, and extensive plasmon resonance bandwidth, rendering it highly appropriate for
162 sensing applications. The relative dielectric properties of Au are delineated by the Drude-Lorentz
163 model [26].

$$\epsilon_{Au}(\omega) = \epsilon_{\infty} - \frac{\omega_D^2}{\omega(\omega + i\gamma_D)} - \frac{\nabla\epsilon \cdot \Omega_L^2}{(\omega^2 - \Omega_L^2) + i\Gamma_L\omega} \quad (1)$$

164 Where ϵ_{Au} , ϵ_{∞} , ω_D , γ_D , Γ_L , $\nabla\epsilon$, and Ω_L are the relative dielectric properties of gold, the
165 high-frequency dielectric property, the plasmon frequency, the damping coefficient, the frequency
166 band width of the Lorentz oscillators, the weighted parameter, and the oscillator strength,
167 respectively, with their values specified in Table 1.

168 **Table 1.** Drude–Lorentz model parameters.

ϵ_{∞}	$\omega_D/2\pi$ (THz)	$\gamma_D/2\pi$ (THz)	$\Gamma_L/2\pi$ (THz)	$\Omega_L/2\pi$ (THz)	$\nabla\epsilon$
5.96730	2113.60	15.920	104.86	650.07	1.09

169 A thin TiO₂ layer is applied as an optical tuning material on the gold coating to modify the
170 local dielectric conditions at the metal-dielectric interface. Its high refractive index enhances
171 electromagnetic field confinement and improves phase matching with the SPP mode, leading to
172 stronger plasmon-analyte interaction and improved refractive index sensitivity. The subsequent
173 equation determines the relation between the wavelength of TiO₂ and its refractive index [27].

$$n_{TiO_2}^2 = 5.913 + \frac{2.441 \times 10^7}{(Wl^2 - 0.803 \times 10^7)} \quad (2)$$

174 In this context, Wl denotes the operational wavelength in angstroms, and the titanium
175 dioxide's RI is n_{TiO_2} .

176 Fused silica serves as the foundational substance of the structure in this research. The RI
177 of Fused silica changes with the wavelength of light, which causes material dispersion when the
178 fiber is in operation. Therefore, it is fundamental to perform numerical simulations to assess how
179 material dispersion affects the PCF's transmission properties. The Sellmeier equation can
180 determine the RI of fused silica [28].



$$n^2(Wl) = 1 + \frac{E_1 Wl^2}{Wl^2 - F_1^2} + \frac{E_2 Wl^2}{Wl^2 - F_2^2} + \frac{E_3 Wl^2}{Wl^2 - F_3^2} \quad (3)$$

181 Where the RI is denoted as n and Wl is the wavelength of fused silica, measured in microns.
182 The dispersion parameters of the Sellmeier equation are given in Table 2.

183 **Table 2.** Sellmeier dispersion parameters.

E_1	E_2	E_3	F_1	F_2	F_3
0.6961663	0.4079426	0.8974794	0.0684043	0.1162414	9.896161

184 The assessment of sensing performance in PCF-based SPR sensors is significantly
185 dependent on the analysis of confinement loss. The subsequent formula can be used to determine
186 the confinement loss [29].

$$\alpha\left(\frac{dB}{cm}\right) = 8.686 \times 10^4 \times \left(\frac{2\pi}{Wl}\right) \times Im(n_{eff}) \quad (4)$$

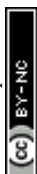
187 Where $Im(n_{eff})$ and Wl denote the fictitious segment of the effective index of the
188 fundamental mode, and the incident wavelength, respectively.

189 The wavelength sensitivity (WS) analysis is a key parameter to assess the sensor's
190 performance. The spectral interrogation approach evaluates sensitivity by observing the shift in
191 resonance wavelength relative to the analyte's RI, mathematically represented as follows [30].

$$WS = \frac{\Delta Wl_{peak}}{\Delta n_a} \left(\frac{nm}{RIU}\right) \quad (5)$$

192 The shift in resonance wavelength, which occurs between two successive peaks, is
193 represented by ΔWl_{peak} and the difference between the two RIs is represented by Δn_a .

194 The sensor performance can be evaluated by another significant measurement called
195 amplitude sensitivity (AS). AS depends on variations in oscillatory strength and recognizes the
196 analyte by assessing the changes in confinement loss. The formula for measuring AS is presented
197 as follows [31]:



$$AS(WL) = -\frac{1}{\alpha(WL, n_a)} \times \frac{\partial \alpha(WL, n_a)}{\partial n_a} (RIU^{-1}) \quad (6)$$

198 The variation in confinement loss between two analytes is $\partial \alpha(WL, n_a)$, and confinement loss
199 for the analyte used for the detection is $\alpha(WL, n_a)$. Within this context, ∂n_a denotes the change
200 between the RIs of analytes that are adjacent.

201 Furthermore, the sensor's figure of merit (FoM) is evaluated to assess the sensing efficacy.
202 The FoM is a quantitative indicator that tells the effectiveness of a sensor, with higher values
203 indicating a higher degree of precision for identifying the RI of a solution. The subsequent equation
204 can be applied to express the FoM [32].

$$FoM = \frac{WS}{FWHM} (RIU^{-1}) \quad (7)$$

205 In this context, WS signifies the wavelength sensitivity, and $FWHM$ refers to the full width
206 at half maximum, indicating the width of the loss spectrum at half of its peak value.

207 Sensor resolution delineates the sensor's capability to perceive deviations in the analyte's
208 RI. This determination is conducted utilizing the following equation [33]:

$$R = \Delta n_a \times \frac{\Delta WL_{min}}{\Delta WL_{peak}} (RIU) \quad (8)$$

209 where, R is the sensor resolution, and ΔWL_{min} represents the smallest possible wavelength
210 resolution.

211 3. Simulation Results and Discussion

212 3.1. Quantitative Findings and Sensitivity Evaluation

213 The evanescent electromagnetic field induced by light traveling within the fiber core is
214 essential in a PCF-based SPR sensor, as it interacts with electrons on the metallic film and enables
215 the excitation of a surface plasmon wave. The optical field is confined and propagates along the
216 core region during light transmission, while the surface plasmon polariton (SPP) mode is generated



217 at the sensing zone, where the plasmonic coating and overlayer are introduced. The operational
218 characteristics depend on the integration of the core mode with the SPP mode. As the first step,
219 we examine the evanescent electromagnetic field profile, which shows a significant coupling
220 between the fundamental mode and the SPP mode for both transverse polarizations (x and y), as
221 presented in Fig. 2 (a)-(d).

222 Fig. 2 (e-f) shows that, for both transverse polarizations (x and y), the plasmonic layer can
223 excite the SPP mode within a certain wavelength range and resonantly interact with the
224 fundamental mode at different frequencies. For x- and y-polarizations, the loss peaks appear at
225 wavelengths of 910 nm and 920 nm, with corresponding confinement losses of 12.95 dB/cm and
226 89.21 dB/cm, respectively. Overall, y-polarization yields a sharper peak profile and a higher loss
227 peak. This indicates that the plasmonic resonance state is more noticeable in y-polarization and
228 that the SPP mode is excited more effectively.

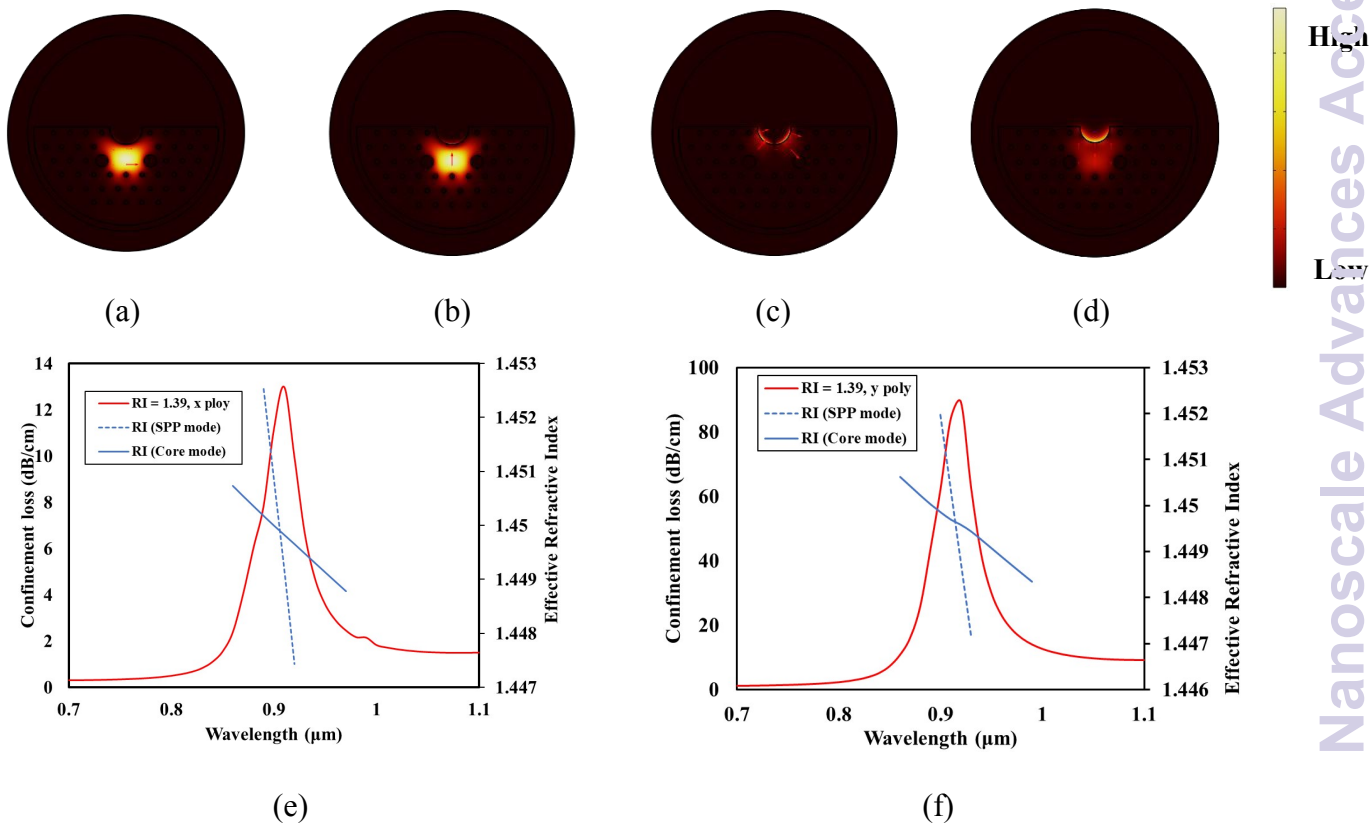


Fig. 2. The electric field profile of (a-b) the fundamental core mode and (b-c) the SPP mode, and dispersion curve of (e-f) confinement loss, fundamental mode, and SPP mode of $n_a = 1.39$, transverse polarizations (x and y), respectively.



229 Since the majority of chemical sensing processes and biochemical interactions usually
 230 occur within the RI ranging from 1.33 to 1.42, this range is chosen for investigation [34], [35]. As
 231 the analyte RI fluctuates between 1.33 and 1.42, Fig. 3(a–b) displays the confinement loss
 232 characteristics for both transverse polarizations (x and y), which are used to evaluate the sensor's
 233 efficiency for multiple analytes. Increasing RI of the analyte induces the resonance peak to redshift
 234 toward higher wavelengths, as shown in Fig. 3 (a–b). A slight change in the RI of the analyte
 235 influences the plasmonic mode's RI, which in turn shifts the phase-matching position. When the
 236 analyte RI changes from 1.41 to 1.42, the resonance wavelength exhibits maximum shifts of 160
 237 nm and 200 nm for transverse polarizations (x and y), respectively. The optimal wavelength
 238 sensitivities achieved at RI =1.41 of 16,000 nm/RIU and 20,000 nm/RIU for the transverse
 239 polarizations (x and y) modes, respectively.

240 The effectiveness of the sensor is further evaluated by determining amplitude sensitivity
 241 using the amplitude measurement approach for both transverse polarizations (x and y), as
 242 displayed in Fig. 3 (c–d). The y-polarization mode demonstrates greater performance (amplitude
 243 sensitivity) than the x-polarization mode, due to a more pronounced loss peak observed in the y-
 244 polarization response. The peak amplitude sensitivities of 653 RIU^{-1} and 1178 RIU^{-1} are measured
 245 for the transverse polarizations (x and y) modes, respectively.

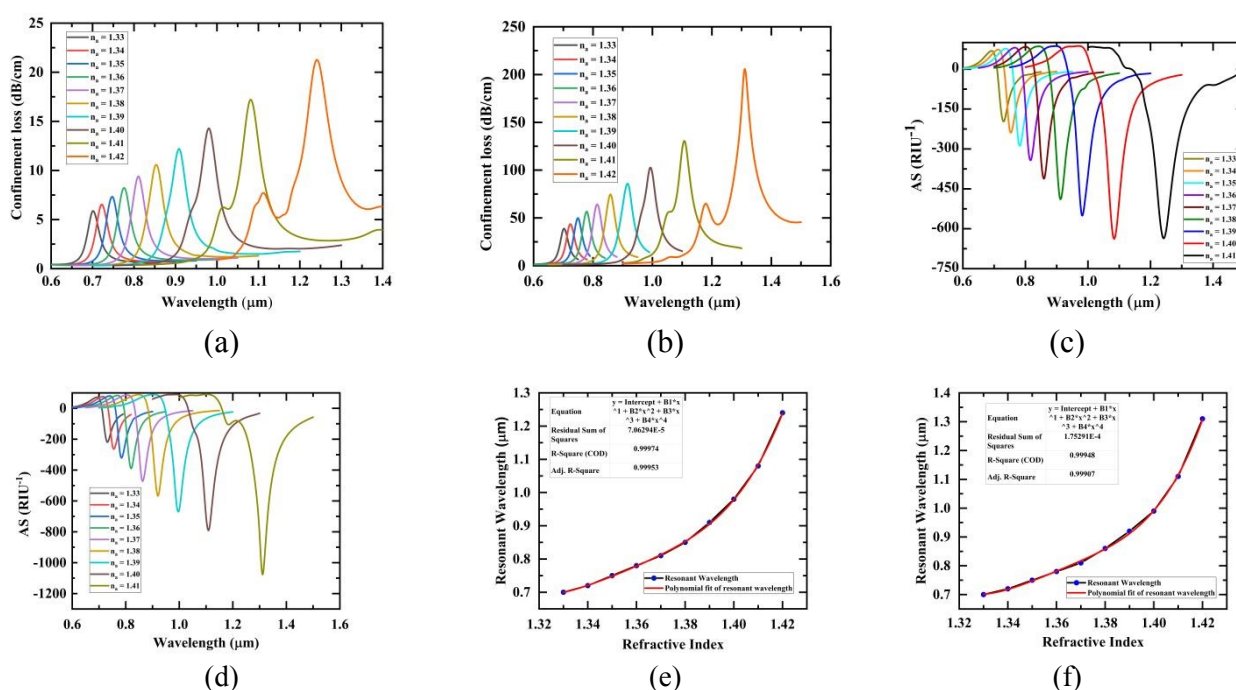


Fig. 3. Dispersion profile of (a-b) confinement loss, (c-d) amplitude sensitivity, and (e-f) fitting polynomials to the resonance wavelengths for an analyte RI variation from 1.33 to 1.42 for transverse polarizations (x and y), respectively.

246 The sensor's performance is quantified using the figure of merit (FoM). A higher FoM
247 signifies superior sensor performance. The estimated FoM values for various analyte RIs are
248 presented in Table 3. The designed sensor obtains a maximum FoM of 265 and 366 for transverse
249 polarization modes (x and y), respectively. Along with sensitivity and FoM, the resolution (R) of
250 the designed sensor is evaluated to provide an in-depth assessment of its performance. The
251 maximum resolutions of 6.25×10^{-6} and 5×10^{-6} (RIU) are observed for the transverse polarization
252 modes (x and y), respectively.

253 The efficacy of a sensor can be assessed by examining the linearity of the fitting curves. A
254 strong association between RI changes and sensor response is reflected by an increased slope of
255 the curve fitting. Fig. 3 (e-f) illustrates the fluctuation in resonance wavelength and the
256 corresponding fitting curves for analyte RI ranging from 1.33 to 1.42. The table displays the
257 parameters and results for the fourth-order fitting.

258 The adjusted R^2 values for the fitted curve of the resonance wavelengths are 0.99953 and
259 0.99907 for transverse polarization modes (x and y), respectively, very close to 1. This indicates
260 that the designed sensor demonstrates exceptional sensing capabilities.

261 **Table 3.** Assessment of sensor performance for amplitude sensitivity and wavelength sensitivity
262 over different analyte refractive index variations.

Analyte RI	Resonant Wavelength (nm)		Wavelength Sensitivity (nm/RIU)		Amplitude Sensitivity (RIU ⁻¹)		FoM (RIU ⁻¹)	
	x-pol	y-pol	x-pol	y-pol	x-pol	y-pol	x-pol	y-pol
1.33	700	700	2000	2000	219	247	66	68
1.34	720	720	3000	3000	265	278	97	99
1.35	750	750	3000	3000	322	346	92	97
1.36	780	780	3000	3000	354	429	87	92
1.37	810	810	4000	5000	445	508	109	142
1.38	850	860	6000	6000	526	615	144	155
1.39	910	920	7000	7000	594	688	149	152
1.4	980	990	10000	12000	658	836	197	215
1.41	1080	1110	16000	20000	653	1178	265	366
1.42	1240	1310						



In all cases, a more defined peak profile with a greater confinement loss is achieved in the y-polarization mode. This indicates that the SPP mode operates more effectively, and the plasmonic resonance state is more prominent in y-polarization. Therefore, in subsequent investigations, we examine the sensor's y-polarization reliability.

Table 4 presents a comparative study of the designed D-shaped PCF-based SPR sensor's performance with existing published PCF-based SPR sensors, emphasizing the key characteristics such as AS, WS, R, and FoM. Our designed D-shaped sensor exhibits excellent performance compared to the other sensors, offering the maximum AS of 1178 RIU⁻¹, the highest WS of 20000 nm/RIU, excellent wavelength resolution of 5×10^{-5} RIU, and a moderate FoM of 366 RIU⁻¹ for y polarization mode. The aforementioned properties make the designed sensor exceptionally effective for accurate and precise refractive index detection.

Table 4. A comparative study of the proposed D-shaped PCF-based SPR sensor's performance with recently reported PCF-based SPR sensors.

Configuration	RI range	Max. WS (nm/RIU)	Max. AS (RIU ⁻¹)	R (RIU)	FOM (RIU ⁻¹)	Ref.
Dual-Channel D-Shaped	1.31–1.41	10,000	216	5×10^{-5}	125	[36]
D-shaped	1.35–1.46	5,600	–	8×10^{-4}	–	[37]
D-Shaped	1.26–1.38	5,400	–	–	–	[38]
Hoop-Cut	1.39–1.44	2,000	374.062	–	–	[39]
Proposed structure	1.33–1.42	20,000	1178	5×10^{-5}	366	

3.2. Variation of Architectural Parameters

This section highlights the sensor functionality by modifying structural parameters. The refractive indices (RIs) of 1.40 and 1.41 were selected as reference values to assess the sensor's performance under variations in geometric parameters. Subsequent investigations were carried out by adjusting these parameters while employing the selected RI values as benchmarks.

3.3. Influence of air space diameters on sensor performance

In a PCF, the air spaces act as the fundamental cladding zone. To enhance the sensor's sensitivity, the influence of geometric parameters was investigated by simulating various air space



284 diameters (d_1 , d_2). The initial assessment focused on the cladding air space (d_1), as depicted in Fig.
 285 1 (a). Fig. 4 (a) demonstrates the loss peak of the structure for RIs of analyte ranging from $n_a =$
 286 1.40 to $n_a = 1.41$. The data indicate that the loss peak increases as d_1 enlarges from 1.1 μm to 1.5
 287 μm , as increasing the diameter of the smaller air space enhances the refractive contrast between
 288 cladding and core, improving phase matching between the SPP and core mode. The findings
 289 indicate that deviations of d_1 from its optimal diameter alter the loss characteristics, thereby
 290 affecting the AS, as illustrated in Fig. 4 (b). Table 4 shows that variations in d_1 do not affect the
 291 resonance wavelength, caused by the strong confinement of the y-polarized mode within the core
 292 region. As indicated by Fig. 4 (a-b) and Table 5, the sensor achieves its peak AS of 1178 nm/RIU
 293 at $d_1=1.1 \mu\text{m}$; therefore, this value was selected as the optimum diameter for the cladding small air
 294 space.

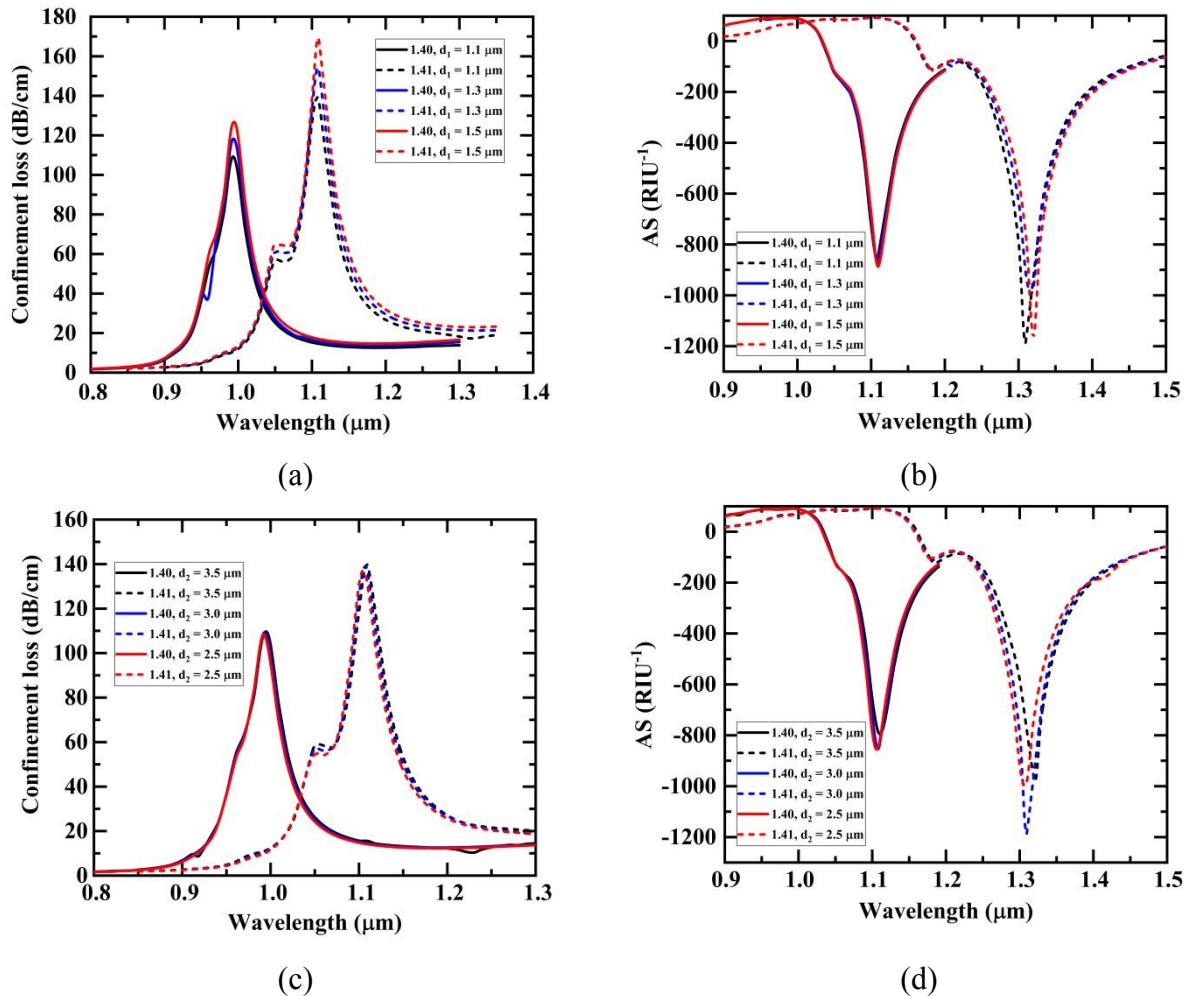


Fig. 4. Effect of the variation in air hole diameter d_1 and d_2 on the sensor's (a-c) confinement loss (b-d) AS for analyte RI varying from 1.40 to 1.41, respectively.



295 Simulations were carried out for $d_2 = 3.5, 3, 2.5 \mu\text{m}$, with the outcomes displayed in
 296 Fig. 4 (c-d) and Table 5. Fig. 4 (c) shows that the peak loss for analyte RIs lies within the
 297 range of 1.40 to 1.41. The study indicates that the loss peak decreases as d_2 increases, and the
 298 loss peak exhibits an upward shift as d_2 decreases. The phenomenon occurs because of a
 299 bigger air space diameter, which effectively confines the core-directed mode, keeping more
 300 of the light within the core and reducing interaction with the metallic film. As a result, the
 301 excitation of surface electrons weakens, lowering the evanescent wave's penetration and the
 302 overall confinement loss. A red shift is also observed with the increase in space size. Fig. 4
 303 (d) presents the amplitude sensitivity (AS) for $n_a = 1.40$ to $n_a = 1.41$. The overall best results
 304 were achieved at $d_2 = 3 \mu\text{m}$.

3.4. Influence of micro-channel on sensor efficacy

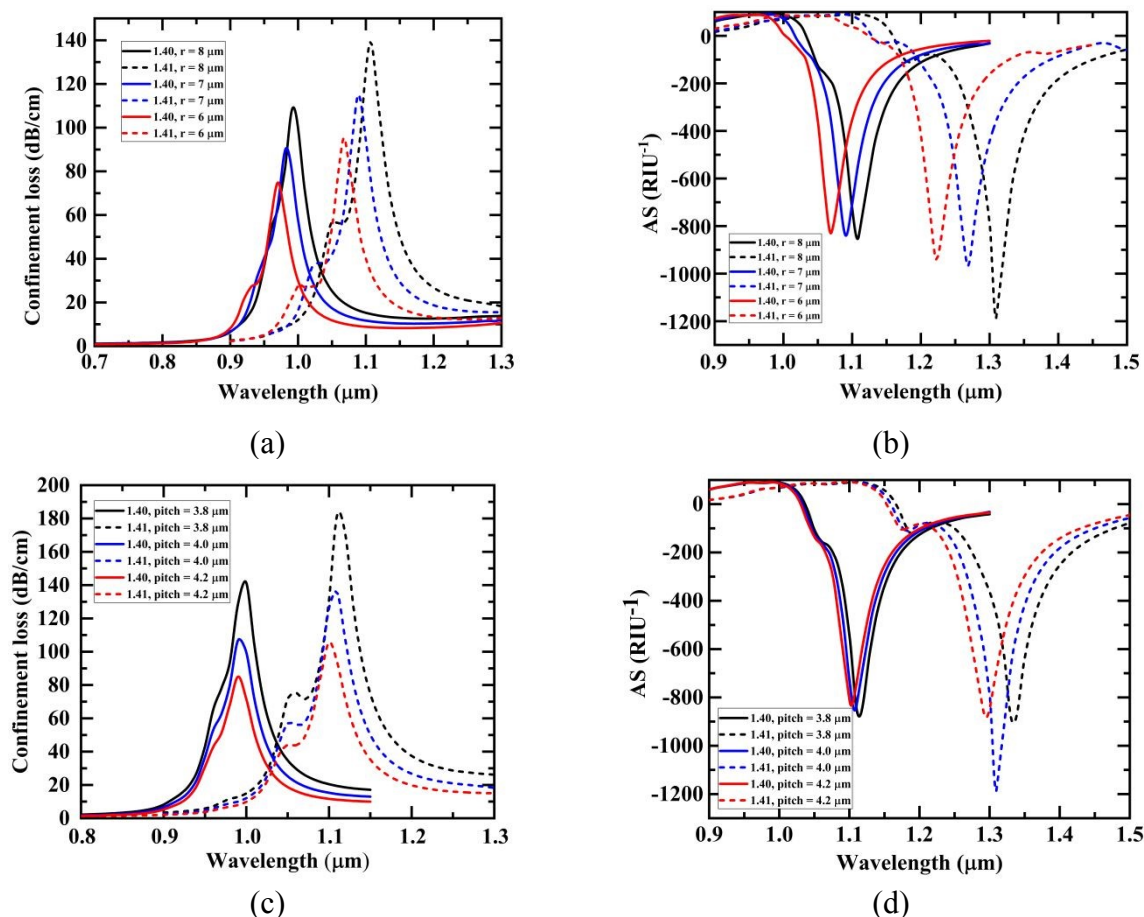


Fig. 5. Effect of the variation in microchannel diameter r and pitch distance on the sensor's (a-c) confinement loss, (b-d) AS for analyte RI varying from 1.40 to 1.41, respectively.



307 The integration of a micro-channel in a D-shaped PCF-based SPR sensor improves analyte
 308 accessibility and boosts the interaction between guided and surface plasmon modes, resulting in
 309 increased resonance depth and sensitivity. Fig. 5 (a) explains the effect of varying the micro-
 310 channel diameter. The micro-channel diameter increases from 6 μm to 8 μm in increments of 0.5
 311 μm . At $r = 8 \mu\text{m}$, the confined loss escalates markedly from 106.88 dB/cm to 135.83 dB/cm as the
 312 RI changes from 1.40 to 1.41, indicating a pronounced sensitivity of loss to small RI shifts in this
 313 range. Fig. 5 (b) illustrates that AS fluctuates considerably with changes in the value of r . The
 314 amplitude sensitivity values for 6, 7, and 8 μm are 913.7, 958.6, and 1178 RIU⁻¹ at $n_a = 1.41$,
 315 respectively. Thus, 8 μm is selected as the optimum micro-channel diameter for the designed
 316 sensor. A detailed summary of the relationship between open channel diameter and sensor
 317 sensitivity is presented in Table 5.

318 **Table 5.** The optimized values for analyte detection range from 1.40 to 1.41.

Diameter (μm)	Wl_{peak} (μm) $n_a=1.40$	Wl_{peak} (μm) $n_a=1.41$	Confinement loss (dB/cm), $n_a=1.40$	Confinement loss (dB/cm), $n_a=1.41$	AS (RIU ⁻¹), $n_a=1.40$	AS (RIU ⁻¹), $n_a=1.41$
d₁						
1.1	0.99	1.11	106.88	135.83	836	1178
1.3	0.99	1.11	114.95	151.69	862	971
1.5	0.99	1.11	122.12	166.71	885	1164
d₂						
3.5	0.99	1.11	105.41	139.10	795	977
3	0.99	1.11	106.88	135.83	836	1178
2.5	0.99	1.1	107.06	130.99	824	977
r						
8	0.99	1.11	106.88	135.83	836	1178
7	0.98	1.09	88.59	114.80	838	958
6	0.97	1.07	74.79	93.42	826	913
Pitch (μm)						
3.8	1.00	1.11	141.45	182.23	842	875
4.0	0.99	1.11	106.88	135.83	836	1178
4.2	0.99	1.10	84.98	105.51	808	848

319 3.5. Impact of pitch on sensor effectiveness

320 Pitch of the air spaces influences the sensing efficacy of the sensor. In this study, the effect
 321 of the pitch variation is also investigated. To achieve optimal sensing performance, we precisely
 322 adjusted the pitch distance by gradually increasing it from 3.8 to 4.2 μm . Fig. 5 (c) illustrates that
 323 the peak confinement loss is achieved at pitch = 3.8 μm , about 141.45 and 182.23 dB/cm for the



324 analyte RI ranging from 1.40 to 1.41, respectively. As the distance increases, the peak loss
325 decreases because the effective mode index differences between the cladding and core increase.
326 Fig. 5 (d) depicts that the amplitude sensitivity obtained for the $\Lambda = 4 \mu\text{m}$ is higher than that of the
327 $\Lambda = 3.8 \mu\text{m}$ and $4.2 \mu\text{m}$. The amplitude sensitivity of 875.53, 1178, and 847.95 RIU^{-1} are achieved
328 for the pitch distances $\Lambda = 3.8, 4,$ and $4.2 \mu\text{m}$, respectively, at $n_a=1.41$. Hence, $4 \mu\text{m}$ is picked as
329 the most efficient pitch distance for the designed sensor. A detailed summary of the relationship
330 between open channel diameter and sensor sensitivity is presented in Table 5.

331 **3.6. Impact of gold (Au) coating depth on sensing efficacy**

332 The gold layer height significantly influences the sensor's effectiveness, as it directly alters
333 the resonance wavelength shift. This effect was assessed by examining variations in Au thickness.
334 Fig. 6 (a) indicates that while the field confinement reduces with increasing Au thickness, the
335 resonance peak experiences only a minor shift towards higher wavelengths for analyte RIs $n_a =$
336 1.40 to $n_a = 1.41$. To investigate the contribution of Au layer height on the confinement loss and
337 the AS, the Au layer height was adjusted between 50 and 60 nm. Observations show, the loss is
338 higher at Au = 50 nm, and lower at Au = 60 nm for analyte RIs $n_a = 1.40$ to $n_a = 1.41$, respectively.
339 Fig. 6 (b) shows that the AS obtained for the 50 nm Au layer is higher than that of the 55 nm and
340 60 nm layers, whereas its WS is lower than that of the 55 nm layer. The 55 nm Au layer exhibits
341 moderate confinement loss along with enhanced AS and WS. Thus, 55 nm is chosen as the
342 optimum Au layer height for the designed sensor. A detailed summary of the correlation between
343 Au layer height and AS is presented in Table 6.

344 **3.7. Impact of TiO_2 coating depth on sensing efficacy**

345 A thin TiO_2 dielectric overlayer modifies the plasmon–analyte interaction by enhancing the
346 propagation of the evanescent electromagnetic field into the analyte medium, thereby improving
347 sensor sensitivity. The confinement loss curve and AS responses for different TiO_2 layer heights
348 are explained in Fig. 6 (c–d). To evaluate the contribution of TiO_2 height on the sensing
349 characteristics, the layer thickness was gradually changed from 10 to 8 nm for analyte RIs
350 extending from 1.40 to 1.41. A wavelength shift of 120 nm was seen in the loss spectrum peak
351 with varying refractive index at a height of 9 nm for TiO_2 , as presented in Fig. 6 (c), yielding the



352 peak WS of 12000 nm/RIU. Fig. 6 (d) indicates that the amplitude sensitivity achieves its highest
 353 value of 1243 RIU⁻¹ at a TiO₂ height of 10 nm, although its wavelength sensitivity is comparatively
 354 lower than that of the 9 nm layer. The 9 nm TiO₂ layer exhibits an optimal trade-off between
 355 confinement loss and sensitivity enhancement, exhibiting both superior wavelength and amplitude
 356 sensitivities with moderate confinement loss. Therefore, a TiO₂ layer height of 9 nm is identified
 357 as the efficient design parameter for the designed sensor. In Table 6, the correlation between the
 358 height of the TiO₂ layer and the associated sensing performance is summarized in detail.

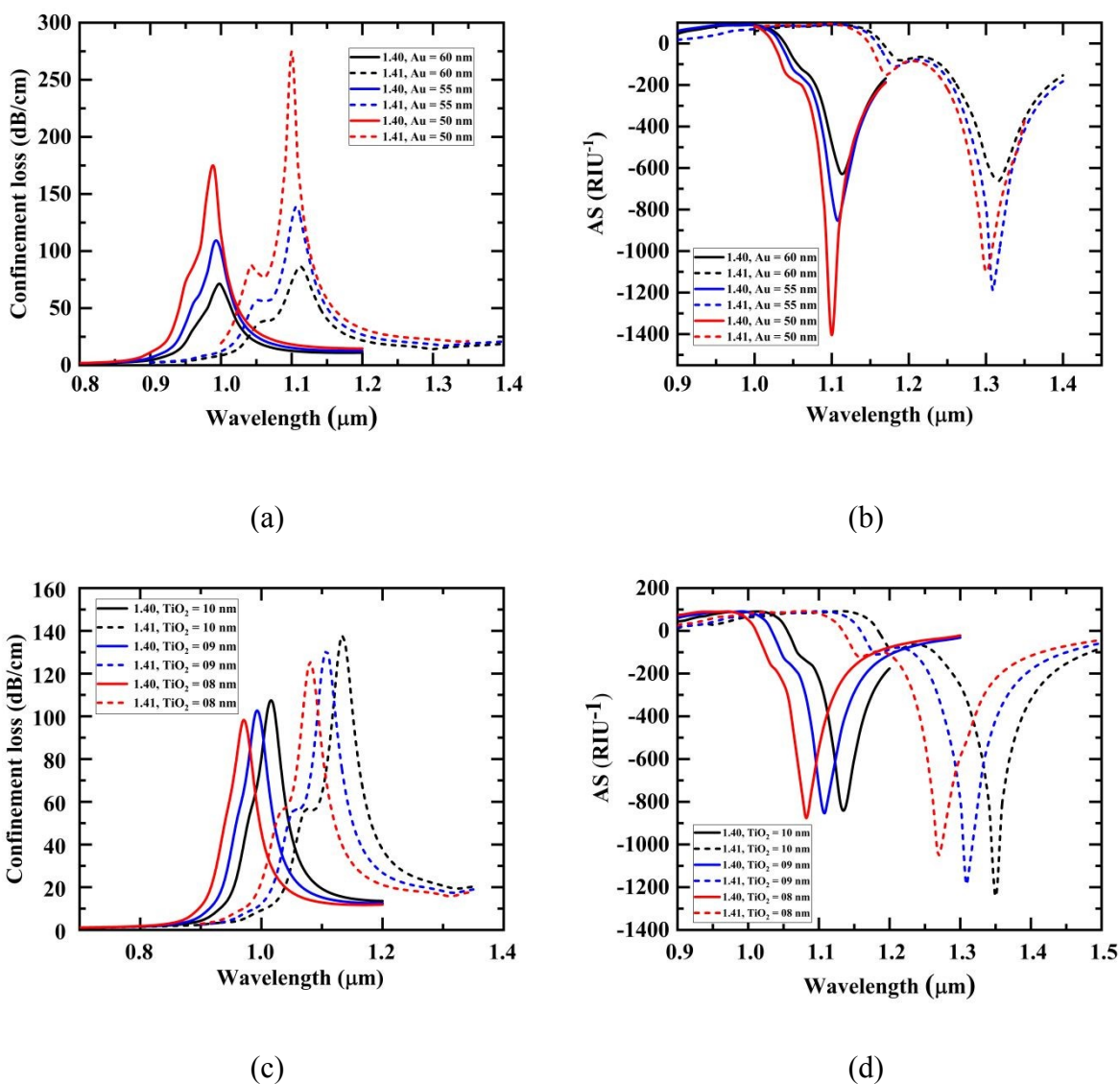


Fig. 6. Impact of the variation in Au and TiO₂ layer height on the sensor's (a-c) confinement loss, (b-d) AS for analyte RI varying from 1.40 to 1.41, respectively.



359 **Table 6.** A thorough explanation of the correlation between the Au and TiO₂ layer height with
360 sensor sensitivity.

Material thickness (nm)	Wl_{peak} (μm) $n_a=1.40$	Wl_{peak} (μm) $n_a=1.41$	Confinement loss (dB/cm), $n_a=1.40$	Confinement loss (dB/cm), $n_a=1.41$	AS (RIU ⁻¹), $n_a=1.40$	AS (RIU ⁻¹), $n_a=1.41$
Au						
60	1.0	1.11	70.33	85.68	612.74	648.65
55	0.99	1.11	106.89	135.83	836.4	1178
50	0.99	1.10	173.75	274.77	1404.69	1099.65
TiO₂						
10	1.02	1.13	110.60	141.70	797.99	1243.24
9	0.99	1.11	106.87	135.83	836.4	1178
8	0.97	1.08	104.43	133.22	851.54	1050.49

361 3.8. Adding Only Gold Coating

362 The simulation uses an Au layer without a TiO₂ overlayer. The findings are displayed in
363 Fig. 7 (a-b) and Table 7. Without an overlayer in the PCF-based SPR sensor design, the peak WS,
364 AS, and FoM reached 12,000 nm/RIU, 987.10 RIU⁻¹, and 219.78 RIU⁻¹ at $n_a = 1.41$, respectively.
365 Although this shows moderate sensitivity, adding an overlayer further improved performance. The
366 overlayer optimizes resonance by enhancing the connection between SPP and guided modes,
367 increasing sensitivity. After adding a TiO₂ overlayer, the sensor achieved the ultimate WS, AS,
368 and FoM of 20,000 nm/RIU, 1178.3 RIU⁻¹, and 366 RIU⁻¹ at $n_a = 1.41$, respectively. This
369 underscores the importance of overlayers in refining the sensor's optical characteristics for better
370 detection efficiency and sensitivity.

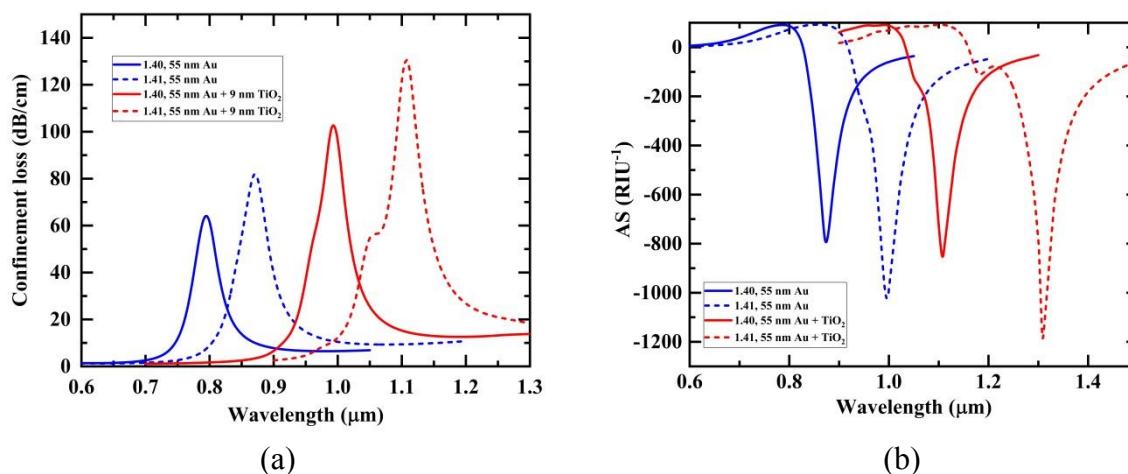
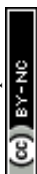


Fig. 7. Dispersion profile of (a) confinement loss and (b) AS for an analyte RI varied from 1.40 to 1.41, when the simulation uses only an Au layer and with a TiO₂ overlayer.



371 **Table 7.** Evaluation of sensor performance for AS and WS over different analyte refractive
372 index variations when the simulation uses only an Au layer and with a TiO₂ overlayer.

Analyte RI	WS (nm/RIU)		AS (RIU ⁻¹)		FoM (RIU ⁻¹)	
	Au	Au+TiO ₂	Au	Au+TiO ₂	Au	Au+TiO ₂
1.33	2000	2000	99.80	247	49.75	68
1.34	1000	3000	132.39	278	26.04	99
1.35	2000	3000	172.25	346	54.35	97
1.36	2000	3000	239.64	429	55.56	92
1.37	3000	5000	323.84	508	84.03	142
1.38	4000	6000	430.69	616	109.59	155
1.39	5000	7000	592.80	689	127.88	152
1.4	8000	12000	758.35	836	178.57	215
1.41	12000	20000	987.10	1178.3	219.78	366
1.42						

373 3.9. Investigation of Fabrication Tolerance

374 These tolerance variations represent practical uncertainties arising during micro-channel
375 formation and Au/TiO₂ thin-film deposition in real fabrication processes. Despite the advancement
376 in the fabrication process, there is still a statistical chance of an inevitable uncertainty that could
377 alter the design variables from their optimal value. So, it is essential to analyze the design tolerance
378 level of the suggested sensor. Therefore, within this segment, the analyte RI value 1.39 is chosen
379 to assess the fabrication tolerance with $\pm 2\%$ variation of the sensor parameters. Fig. 8 (a) illustrates
380 the confinement loss curve due to $\pm 2\%$ variation of the pitch from its optimal value. With 2%
381 decrease in the pitch from the optimal level, the loss increases, and with 2% increment, the loss
382 decreases. However, shows no variation in the resonant wavelength of 920 nm in both cases. Fig.
383 8 (b) shows that $\pm 2\%$ variation in the Au film thickness (t_{Au}) from its optimum value influences
384 the loss curve. As demonstrated in Fig. 8 (b), the resonant wavelength remained unchanged at 920
385 nm, and confinement loss varies as the thickness changes by $\pm 2\%$ from its original value. The
386 confinement loss grows from 89.21 to 95.17 dB/cm, by 2% decrease in gold thickness, and by 2%
387 increase, loss decreases from 89.21 to 82.79 dB/cm. Furthermore, due to $\pm 2\%$ deviation of the air
388 space d_1 and d_2 , there is no significant movement in the loss curve, and the loss curve is almost
389 identical, depicted in Fig. 8 (c-d), respectively. From this study, the resonant wavelength remained
390 unchanged at 920 nm for analyte RI 1.39, with only minor variations in confinement loss. This



391 confirms that the proposed sensor is highly robust against $\pm 2\%$ variations in structural parameters
392 and that the simulated performance can be reliably translated to practical fabrication scenarios.

393 Despite the promising numerical performance, especially the sensitivity of the proposed
394 sensor, certain limitations should be acknowledged. This study does not consider the effects of
395 other practical factors, such as temperature variations, measurement noise, and spectral broadening
396 are not included in the simulations. These aspects can be evaluated in future work.

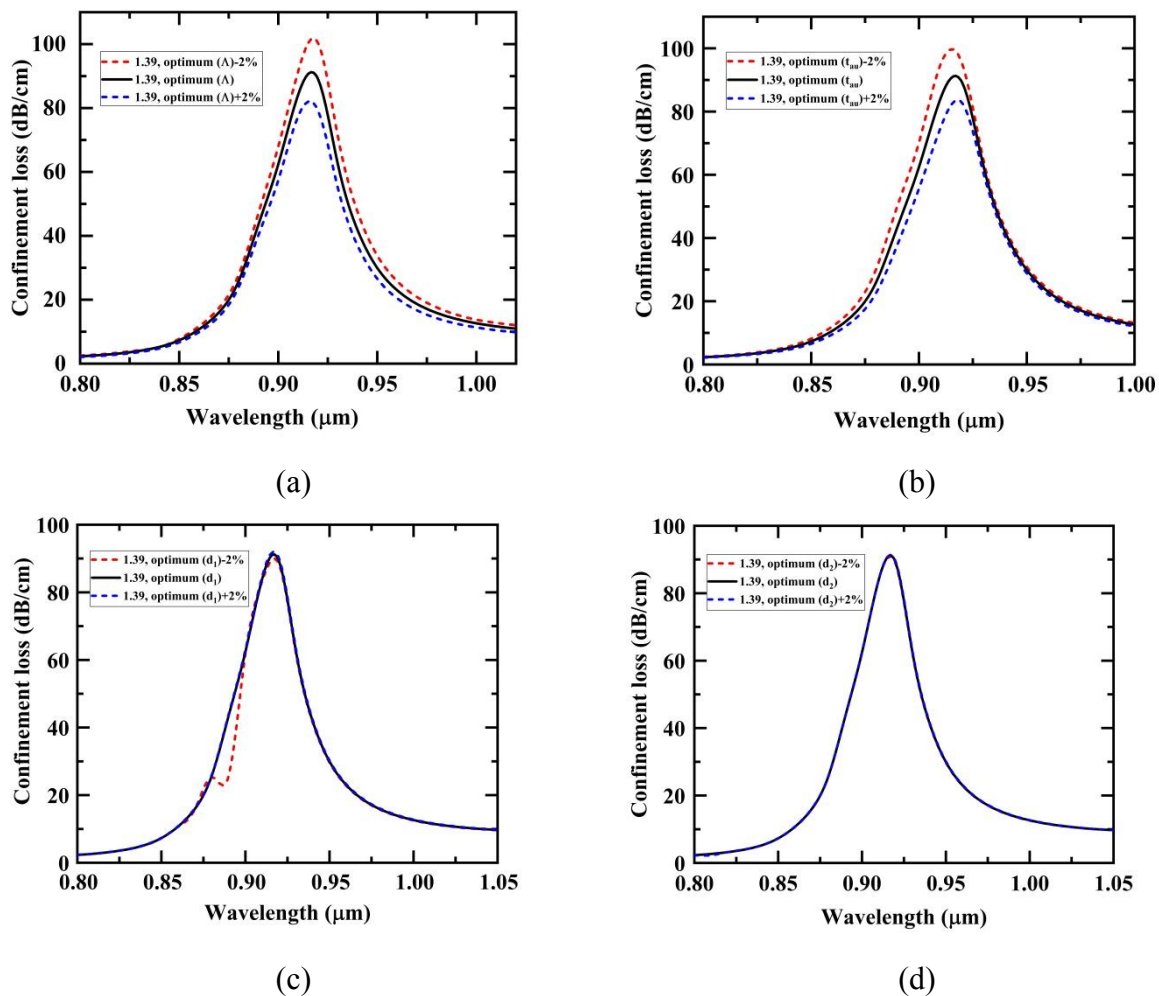


Fig. 8. Fabrication tolerance investigation for $\pm 2\%$ deviation of (a) pitch (Λ), (b) Au layer thickness (t_{au}), (c) diameter of air space (d_1), and (d) diameter of air space (d_2).

397 3.10. Evaluation of the fabrication feasibility of the proposed PCF sensor

398 The fabrication viability of PCFs is investigated in this section, with a focus on the
399 possibility of developing a particular fiber structure. Compared to conventional fibers, PCFs are



400 more beneficial; several methods are utilized for the fabrication of the sensor, including stack-and-
 401 draw procedures, die-casting technique, and sol-gel processing [40]. The fabrication procedures
 402 for the micro-channel-based D-shaped sensor are demonstrated in Fig. 9 (a). Complex shapes such
 403 as circular, triangular, and square lattices can be easily created using the stack-and-draw procedure,
 404 which offers an extensible and versatile approach for the fabrication of PCFs. In this structure, thin
 405 and thick capillaries are employed to generate large and tiny air spaces, wherein guiding cores are
 406 created by swapping a capillary with a solid rod and then removing these rods entirely [41], [42].
 407 After the fabrication of PCF, TiO₂ and Au layers on the PCF can be easily coated through various
 408 deposition techniques, such as the Chemical Vapor Deposition method and Atomic Layer
 409 Deposition (ALD) [43], [44]. The unidentified analyte can be detected by analyzing the
 410 confinement loss of the sensor.

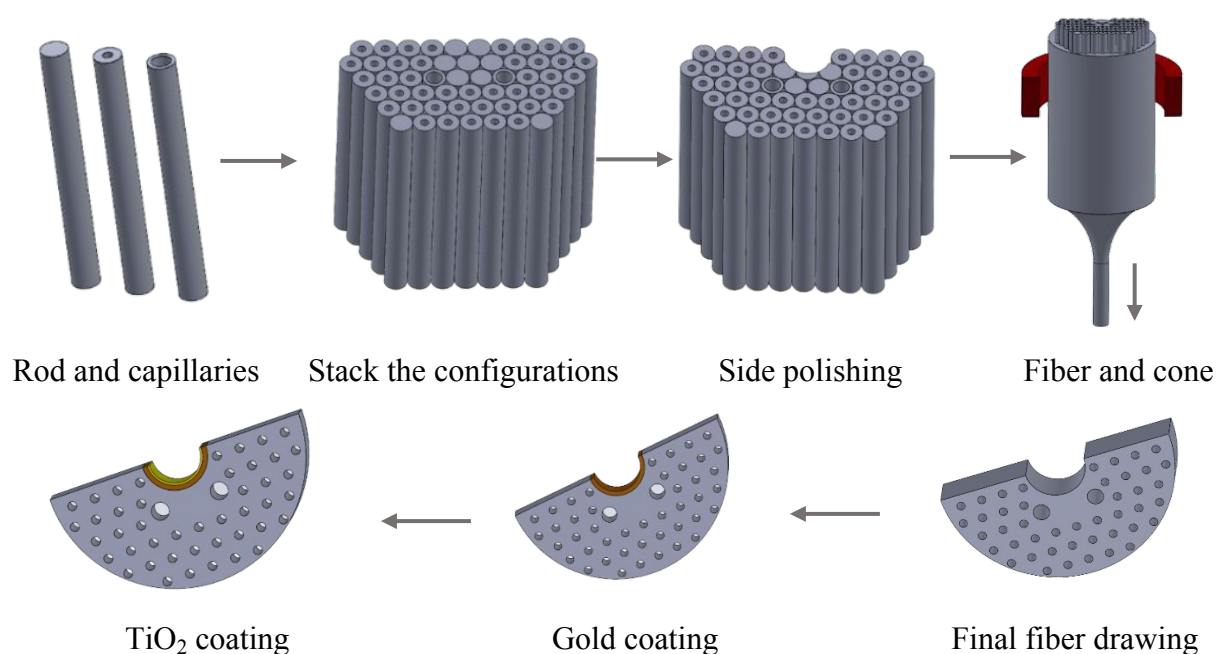
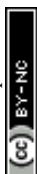


Fig. 9. Schematic of the designed sensor fabrication process.

411

Table 8. The RI variation for Healthy cells and Cancerous cells.

Cell Name	Cell Type and Concentration Level	RI		Ref.
		Healthy cell	Cancerous cell	
Basal cell	(30–70%) Non-malignant cell (80%) Malignant skin lesion	1.360	1.380	[45], [46]
HeLa	(30–70%) Non-malignant cell	1.368	1.392	[45], [46]



	(80%) Cervical carcinoma			
Jurkat	(30–70%) Non-malignant cell (80%) Blood malignancy	1.376	1.390	[45], [46]
PC12	(30–70%) Non-malignant cell (80%) Adrenal carcinoma	1.381	1.395	[46], [47]
MDA-MB-231	(30–70%) Non-malignant cell (80%) Mammary carcinoma	1.385	1.399	[46], [47]
MCF-7	(30–70%) Non-malignant cell (80%) Mammary carcinoma	1.387	1.401	[46], [47]

412 3.11. Biomedical Application

413 This segment presents the optical responses at different wavelengths for both non-
 414 malignant and diseased biological samples, incorporating six different carcinoma cell types,
 415 utilizing the refractive indices from Table 8. The confinement loss performance of the D-shape
 416 PCF-based SPR sensor is shown in Fig. 10 (a–f) for a variety of biological samples, such as Basal,
 417 HeLa, Jurkat, PC12, and mammary carcinoma cell types MDA-MB-231 and MCF-7. The red line
 418 in every scenario denotes malignant cells, whereas the black line shows normal (healthy) cells.
 419 These differences in refractive index, originating from cellular variations such as cytoplasmic
 420 density and membrane composition, produce distinct plasmonic resonance shifts, enabling clear
 421 discrimination between healthy and malignant cells.

422 In every scenario, carcinoma cells show higher confinement losses and redshifted
 423 resonance peaks in comparison to their normal counterparts. One of the most frequently employed
 424 means for assessing sensor efficacy is spectral interrogation, which is based on the variations in
 425 resonance peaks across the wavelength spectrum. This idea can be clarified by applying equation
 426 (5), which examines wavelength changes associated with the loss peak and refractive index
 427 variations. Additionally, sensor effectiveness can be evaluated using the amplitude sensitivity at a
 428 particular wavelength, as calculated using Eq. (6). Based on the cancer cell types that were studied,
 429 the spectral sensitivities were 4000, 5000, 5714.29, 6428.57, 6428.57, and 7142.86 nm/RIU for
 430 Basal, HeLa, Jurkat, PC12, MDA-MB-231, and MCF-7 cells, while the corresponding amplitude
 431 sensitivities were 580.15, 628.57, 640.34, 669.29, 717.29, and 708.02 RIU⁻¹, respectively. Fig. 11
 432 and Table 9 provide detailed information regarding the sensor's performance, including sensitivity,
 433 figure of merit (FOM), and resolution for six different types of carcinoma cells. The designed D-
 434 shaped sensor exhibits remarkable sensitivity, figure of merit, and resolution, signifying that this



435 sensor delivers superior response. Moreover, it should be noted that all analyses, including cancer
 436 detection, are based on FEM simulations; experimental validation is the necessary next step to
 437 confirm the sensor's performance in real world sample detection.

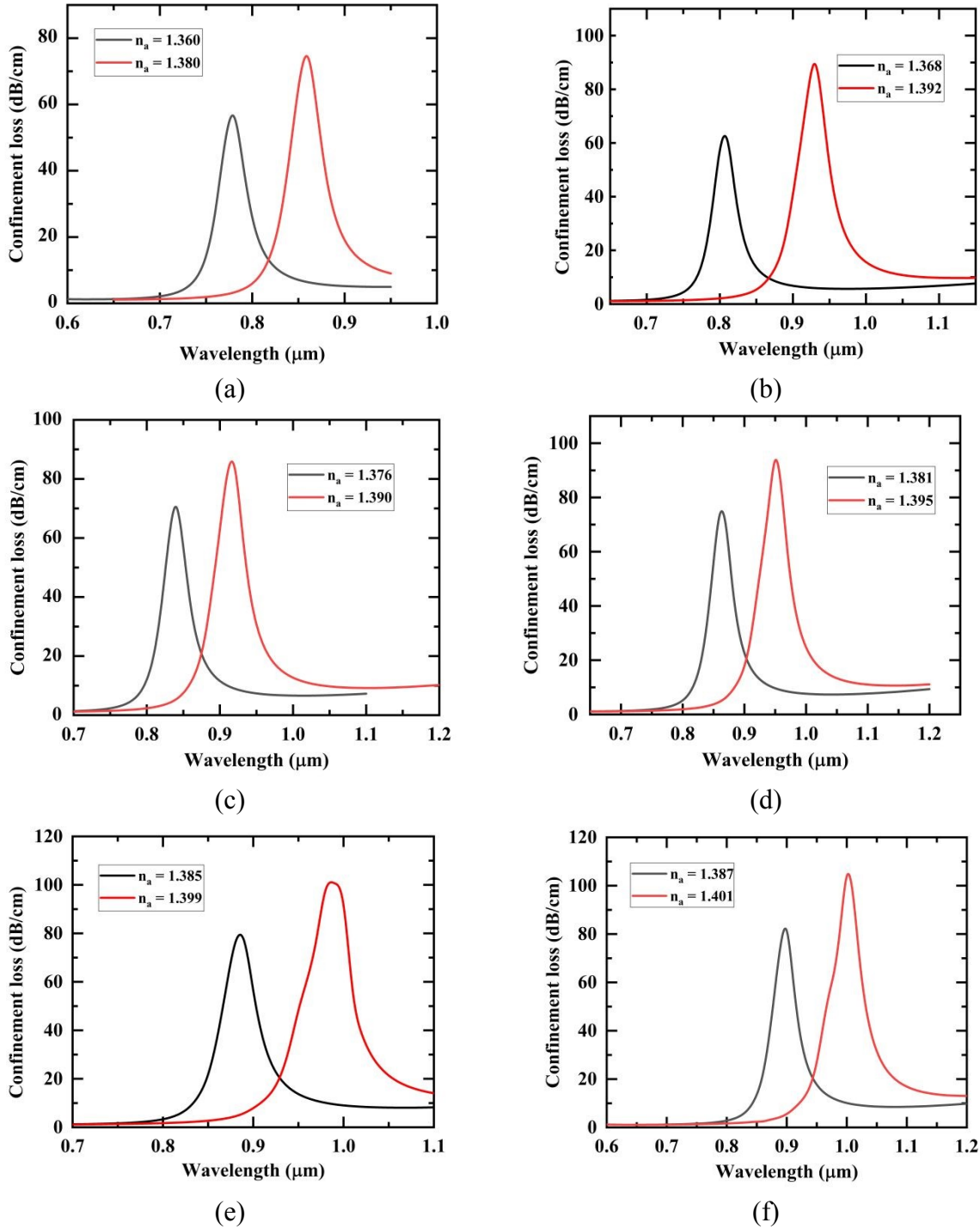


Fig. 10. (a-f) Outcomes of the identification of malignant skin lesions, cervical carcinoma, blood malignancy, adrenal carcinoma, and two variants of mammary carcinoma (MDA-MB-231 and MCF-7) utilizing the designed sensor.



438

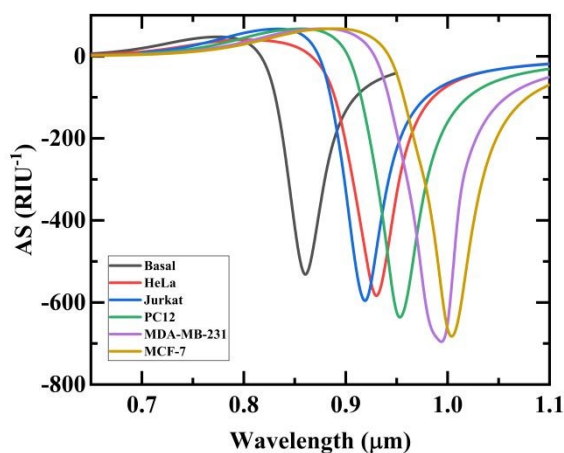


Fig. 11. AS for the following six carcinoma cell types: PC12, MDA-MB-231, Jurkat, HeLa, Basal, and MCF-7.

439 **Table 9.** Assessment of the Sensor's effectiveness at refined design variables for identifying
440 different carcinoma cell types.

Cancer type	Cell type	WS (nm/RIU)	AS (RIU ⁻¹)	FOM (RIU ⁻¹)	Resolution (RIU)
Skin	Basal	4000.00	580.15	122.70	2.5×10^{-5}
Cervical	HeLa	5000.00	628.57	144.93	2.0×10^{-5}
Blood	Jurkat	5714.29	640.34	155.28	1.75×10^{-5}
Adrenal gland	PC12	6428.57	669.29	159.91	1.56×10^{-5}
Breast	MDA-MB-231	6428.57	717.29	153.06	1.56×10^{-5}
Breast	MCF-7	7142.86	708.02	165.34	1.40×10^{-5}

441

442 4. Conclusion

443 Accurate and early detection of cancer plays a vital role in enhancing patient outcomes,
444 and non-invasive diagnostic techniques are making significant advances to address this issue.
445 Among various non-invasive optical tools, D-shaped PCF-based SPR sensors are at the forefront
446 due to their excellent sensitivity and fabrication simplicity. This study has designed a PCF-based
447 SPR sensor for the identification of various carcinoma cells utilizing a D-shaped structure. The
448 spectral and amplitude interrogation methods have been employed to investigate the performance
449 of different sensor configurations. The impact of incorporating multiple air holes and their size,
450 diameter, pitch distance, along with the impact of adding a plasmonic layer, TiO₂ overlayer, and
451 their thickness on sensor performance has been comprehensively analyzed to obtain the optimized



452 structure. The sensor achieved the highest amplitude and spectral sensitivities of 717.29 RIU⁻¹ and
453 7142.86 nm/RIU, respectively, recorded for MCF-7 and MDA-MB-231 cells. Additionally, the
454 designed sensor exhibited the highest spectral sensitivity of 20,000 nm/RIU across the RI span of
455 1.330 to 1.420 for y-polarized light. The sensor also depicted outstanding FOM, AS, and resolution
456 values of 366 RIU⁻¹, 1178 RIU⁻¹, and 5×10⁻⁶ RIU, respectively, within the aforementioned RI
457 range. Finally, a convenient and effective way of the presented sensor's fabrication is proposed
458 with a detailed analysis of fabrication feasibility via investigating its fabrication tolerance. The
459 outcomes of the simulation show an impressive improvement in sensitivity and accuracy compared
460 to the state-of-the-art studies in the literature, which is a testament that the designed architecture
461 could be an effective tool for the precise diagnosis of cancer with better resolution. It should be
462 noted that all analyses, including cancer-cell detection and fabrication-tolerance evaluation, are
463 based on FEM simulations; experimental validation is required to confirm the sensor's
464 performance in real biological environments.

465 **CRedit authorship contribution statement**

466 Kazi Zannatul Ferdushee : Writing – original draft, Software, Formal analysis, Methodology,
467 Visualization. Md Abu Shahid Chowdhury: Conceptualization, Supervision, Writing – original
468 draft, Formal analysis, Validation, Visualization. Siddika Tamanna Islam: Writing – review &
469 editing.

470 **Conflicts of Interest**

471 The authors declare they have no conflicts of interests.

472 **Data availability statement**

473 The data that support the findings of this study will be made available from the corresponding
474 author upon reasonable request.

475 **References**

- 476 [1] M. A. Huraiya, S. G. Ramaraj, Sk. Md. Shahadat Hossain, K. Chakrabarti, H. Tabata, and S. M. A. Razzak, "A
477 highly optimized and sensitive bowtie shape-based SPR biosensor for different analyte detection," *Nanoscale*
478 *Adv.*, vol. 7, no. 3, pp. 899–908, 2025, doi: 10.1039/D4NA00812J.



- 479 [2] W. Zhu *et al.*, “High confidence plasmonic sensor based on photonic crystal fibers with a U-shaped detection
480 channel,” *Phys. Chem. Chem. Phys.*, vol. 25, no. 12, pp. 8583–8591, 2023, doi: 10.1039/D2CP04605A.
- 481 [3] W. Zhu *et al.*, “Highly sensitive plasmonic sensor based on eccentric-core photonic crystal fibers,” *Phys. Chem.
482 Chem. Phys.*, vol. 25, no. 29, pp. 19596–19605, 2023, doi: 10.1039/D3CP01615C.
- 483 [4] R. L. Siegel, T. B. Kratzer, A. N. Giaquinto, H. Sung, and A. Jemal, “Cancer statistics, 2025,” *CA. Cancer J.
484 Clin.*, vol. 75, no. 1, pp. 10–45, Jan. 2025, doi: 10.3322/caac.21871.
- 485 [5] A. Saha, M. T. Rahman, and B. Dey, “A high-performance BaTiO₃/Ag/BP-based plasmonic biosensor for
486 label-free detection of cancer biomarkers,” *Sens. Actuators Phys.*, vol. 396, p. 117121, Dec. 2025, doi:
487 10.1016/j.sna.2025.117121.
- 488 [6] F. Bray *et al.*, “Global cancer statistics 2022: GLOBOCAN estimates of incidence and mortality worldwide for
489 36 cancers in 185 countries,” *CA. Cancer J. Clin.*, vol. 74, no. 3, pp. 229–263, May 2024, doi:
490 10.3322/caac.21834.
- 491 [7] H. M. Rai and J. Yoo, “A comprehensive analysis of recent advancements in cancer detection using machine
492 learning and deep learning models for improved diagnostics,” *J. Cancer Res. Clin. Oncol.*, vol. 149, no. 15, pp.
493 14365–14408, Nov. 2023, doi: 10.1007/s00432-023-05216-w.
- 494 [8] A. Thamilselvan and M. I. Kim, “Recent advances on nanozyme-based electrochemical biosensors for cancer
495 biomarker detection,” *TrAC Trends Anal. Chem.*, vol. 177, p. 117815, Aug. 2024, doi:
496 10.1016/j.trac.2024.117815.
- 497 [9] V. S. P. K. S. A. Jayanthi, A. B. Das, and U. Saxena, “Recent advances in biosensor development for the
498 detection of cancer biomarkers,” *Biosens. Bioelectron.*, vol. 91, pp. 15–23, May 2017, doi:
499 10.1016/j.bios.2016.12.014.
- 500 [10] S. Kumar and R. Singh, “Recent optical sensing technologies for the detection of various biomolecules:
501 Review,” *Opt. Laser Technol.*, vol. 134, p. 106620, Feb. 2021, doi: 10.1016/j.optlastec.2020.106620.
- 502 [11] R. Zhang, J. Jiang, and W. Wu, “Wearable chemical sensors based on 2D materials for healthcare applications,”
503 *Nanoscale*, vol. 15, no. 7, pp. 3079–3105, 2023, doi: 10.1039/D2NR05447G.
- 504 [12] A. S. Chowdhury, Md. A. Islam, Md. S. Islam, B. Dey, and J. Park, “Design and Analysis of PtSe₂ and Blue
505 Phosphorus/MoS₂ Heterostructure-Based SPR Biosensor,” *ACS Appl. Opt. Mater.*, vol. 2, no. 6, pp. 1046–1059,
506 Jun. 2024, doi: 10.1021/acsaom.4c00050.
- 507 [13] A. Khodaie and H. Heidarzadeh, “Ultra-sensitive surface plasmon resonance sensor integrating MXene
508 (Ti₃C₂TX) and graphene for advanced carcinoembryonic antigen detection,” *Sci. Rep.*, vol. 15, no. 1, p. 13571,
509 Apr. 2025, doi: 10.1038/s41598-025-97853-z.
- 510 [14] A. K. Sharma, R. Jha, and B. D. Gupta, “Fiber-Optic Sensors Based on Surface Plasmon Resonance: A
511 Comprehensive Review,” *IEEE Sens. J.*, vol. 7, no. 8, pp. 1118–1129, Aug. 2007, doi:
512 10.1109/JSEN.2007.897946.
- 513 [15] A. Ramola, A. K. Shakya, A. Droby, and A. Bergman, “Numerical Study of a Novel Kagome-Inspired Photonic
514 Crystal Fiber-Based Surface Plasmon Resonance Biosensor for Detection of Blood Components and Analytical
515 Targets,” *Biosensors*, vol. 15, no. 8, p. 539, Aug. 2025, doi: 10.3390/bios15080539.
- 516 [16] A. Ramola, A. K. Shakya, A. Vidyarthi, S. Singh, E. Talker, and A. Bergman, “Next-generation photonic-
517 crystal-fiber-based plasmonic sensor for heavy metal detection via spectroscopy and refractive index
518 integration,” in *29th International Conference on Optical Fiber Sensors*, M. Lopez-Amo Sainz, J. L. Santos,
519 and T. Sun, Eds., Porto, Portugal: SPIE, May 2025, p. 489. doi: 10.1117/12.3062891.
- 520 [17] A. Ramola, A. K. Shakya, and A. Bergman, “Comprehensive Analysis of Advancement in Optical Biosensing
521 Techniques for Early Detection of Cancerous Cells,” *Biosensors*, vol. 15, no. 5, p. 292, May 2025, doi:
522 10.3390/bios15050292.
- 523 [18] A. Ramola, A. K. Shakya, V. Kumar, and A. Bergman, “Recent Advances in Photonic Crystal Fiber-Based SPR
524 Biosensors: Design Strategies, Plasmonic Materials, and Applications,” *Micromachines*, vol. 16, no. 7, p. 747,
525 Jun. 2025, doi: 10.3390/mi16070747.
- 526 [19] A. Ramola, A. K. Shakya, and A. Bergman, “Finite Element Method-Based Modeling of a Novel Square
527 Photonic Crystal Fiber Surface Plasmon Resonance Sensor with a Au–TiO₂ Interface and the Relevance of
528 Artificial Intelligence Techniques in Sensor Optimization,” *Photonics*, vol. 12, no. 6, p. 565, Jun. 2025, doi:
529 10.3390/photonics12060565.
- 530 [20] M. Ashrafian, S. Olyaei, and M. Seifouri, “Highly sensitive cancer detection using an open D-channel PCF-
531 based SPR biosensor,” *Sci. Rep.*, vol. 15, no. 1, p. 10168, Mar. 2025, doi: 10.1038/s41598-025-95249-7.
- 532 [21] J. M. Nijhum and T. Ahmed, “Highly sensitive quasi-D-shaped photonic crystal fiber biosensor designed for
533 the detection of RBC parasitized by Plasmodium falciparum for the early diagnosis of malaria,” *Opt. Contin.*,
534 vol. 2, no. 6, p. 1315, Jun. 2023, doi: 10.1364/OPTCON.489682.



- 535 [22] J. Divya, S. Selvendran, A. S. Raja, and V. Borra, "A Novel Plasmonic Sensor Based on Dual-Channel D-
536 Shaped Photonic Crystal Fiber for Enhanced Sensitivity in Simultaneous Detection of Different Analytes,"
537 *IEEE Trans. NanoBioscience*, vol. 23, no. 1, pp. 127–139, Jan. 2024, doi: 10.1109/TNB.2023.3294330.
- 538 [23] D. Zhou, F. Ren, Y. Li, Y. Ci, and J. Wang, "A Broadband D-Shaped Photonic Crystal Fiber Sensor via Surface
539 Plasmon Resonance for Different Analytes with a Large Range of Refractive Index Detection," *Plasmonics*,
540 vol. 20, no. 4, pp. 1991–2001, Jul. 2024, doi: 10.1007/s11468-024-02425-y.
- 541 [24] A. Oudenani and A. Sonne, "A D-Shaped SPR-Based PCF Bio-sensor with a High Sensitivity for Wide
542 Refractive Index Detection," *Plasmonics*, vol. 20, no. 7, pp. 5245–5253, Dec. 2024, doi: 10.1007/s11468-024-
543 02689-4.
- 544 [25] M. Azadi, M. Seifouri, S. Olyaei, and M. Mohammadi, "Ultrahigh-sensitivity D-shaped PCF-SPR biosensor
545 with TiO₂-Au hybrid layers for precise detection of blood constituents," *Results Phys.*, vol. 77, p. 108463, Oct.
546 2025, doi: 10.1016/j.rinp.2025.108463.
- 547 [26] A. Vial, A.-S. Grimault, D. Macías, D. Barchiesi, and M. L. De La Chapelle, "Improved analytical fit of gold
548 dispersion: Application to the modeling of extinction spectra with a finite-difference time-domain method,"
549 *Phys. Rev. B*, vol. 71, no. 8, p. 085416, Feb. 2005, doi: 10.1103/PhysRevB.71.085416.
- 550 [27] J. R. DeVore, "Refractive Indices of Rutile and Sphalerite," *J. Opt. Soc. Am.*, vol. 41, no. 6, p. 416, Jun. 1951,
551 doi: 10.1364/JOSA.41.000416.
- 552 [28] I. H. Malitson, "Interspecimen Comparison of the Refractive Index of Fused Silica*,†," *J. Opt. Soc. Am.*, vol.
553 55, no. 10, p. 1205, Oct. 1965, doi: 10.1364/JOSA.55.001205.
- 554 [29] T. P. White, R. C. McPhedran, C. M. De Sterke, L. C. Botten, and M. J. Steel, "Confinement losses in
555 microstructured optical fibers," *Opt. Lett.*, vol. 26, no. 21, p. 1660, Nov. 2001, doi: 10.1364/OL.26.001660.
- 556 [30] A. A. Rifat, G. A. Mahdiraji, Y. M. Sua, R. Ahmed, Y. G. Shee, and F. R. M. Adikan, "Highly sensitive multi-
557 core flat fiber surface plasmon resonance refractive index sensor," *Opt. Express*, vol. 24, no. 3, p. 2485, Feb.
558 2016, doi: 10.1364/OE.24.002485.
- 559 [31] M. Hautakorpi, M. Mattinen, and H. Ludvigsen, "Surface-plasmon-resonance sensor based on three-hole
560 microstructured optical fiber," *Opt. Express*, vol. 16, no. 12, p. 8427, Jun. 2008, doi: 10.1364/OE.16.008427.
- 561 [32] Md. A. Mollah, S. M. R. Islam, Md. Yousufali, L. F. Abdulrazak, Mb. B. Hossain, and I. S. Amiri, "Plasmonic
562 temperature sensor using D-shaped photonic crystal fiber," *Results Phys.*, vol. 16, p. 102966, Mar. 2020, doi:
563 10.1016/j.rinp.2020.102966.
- 564 [33] M. Hautakorpi, M. Mattinen, and H. Ludvigsen, "Surface-plasmon-resonance sensor based on three-hole
565 microstructured optical fiber," *Opt. Express*, vol. 16, no. 12, p. 8427, Jun. 2008, doi: 10.1364/OE.16.008427.
- 566 [34] A. Aray *et al.*, "SPR-based plastic optical fibre biosensor for the detection of C-reactive protein in serum," *J.*
567 *Biophotonics*, vol. 9, no. 10, pp. 1077–1084, Oct. 2016, doi: 10.1002/jbio.201500315.
- 568 [35] A. K. Yetisen *et al.*, "Color-Selective 2.5D Holograms on Large-Area Flexible Substrates for Sensing and
569 Multilevel Security," *Adv. Opt. Mater.*, vol. 4, no. 10, pp. 1589–1600, Oct. 2016, doi:
570 10.1002/adom.201600162.
- 571 [36] J. Divya, S. Selvendran, A. S. Raja, and V. Borra, "A Novel Plasmonic Sensor Based on Dual-Channel D-
572 Shaped Photonic Crystal Fiber for Enhanced Sensitivity in Simultaneous Detection of Different Analytes,"
573 *IEEE Trans. NanoBioscience*, vol. 23, no. 1, pp. 127–139, Jan. 2024, doi: 10.1109/TNB.2023.3294330.
- 574 [37] D. Zhou, F. Ren, Y. Li, Y. Ci, and J. Wang, "A Broadband D-Shaped Photonic Crystal Fiber Sensor via Surface
575 Plasmon Resonance for Different Analytes with a Large Range of Refractive Index Detection," *Plasmonics*,
576 vol. 20, no. 4, pp. 1991–2001, Jul. 2024, doi: 10.1007/s11468-024-02425-y.
- 577 [38] X. Lu, X. Yu, J. Zhou, M. Chang, and D. Lu, "An Ultra-Wide Range D-Shaped Fiber SPR Sensor with a
578 Nanostructure of Gold-MoS₂ and Sodium for the Simultaneous Measurement of Refractive Index and
579 Temperature," *Sensors*, vol. 25, no. 2, p. 377, Jan. 2025, doi: 10.3390/s25020377.
- 580 [39] S. Mittal *et al.*, "Design and Performance Analysis of a Novel Hoop-Cut SPR-PCF Sensor for High Sensitivity
581 and Broad Range Sensing Applications," *IEEE Sens. J.*, vol. 24, no. 3, pp. 2697–2704, Feb. 2024, doi:
582 10.1109/JSEN.2023.3339813.
- 583 [40] D. Pysz *et al.*, "Stack and draw fabrication of soft glass microstructured fiber optics," *Bull. Pol. Acad. Sci.*
584 *Tech. Sci.*, vol. 62, no. 4, pp. 667–682, Dec. 2014, doi: 10.2478/bpasts-2014-0073.
- 585 [41] A. A. Rifat, F. Haider, R. Ahmed, G. A. Mahdiraji, F. R. Mahamd Adikan, and A. E. Miroshnichenko, "Highly
586 sensitive selectively coated photonic crystal fiber-based plasmonic sensor," *Opt. Lett.*, vol. 43, no. 4, p. 891,
587 Feb. 2018, doi: 10.1364/OL.43.000891.
- 588 [42] D. J. J. Hu and H. P. Ho, "Recent advances in plasmonic photonic crystal fibers: design, fabrication and
589 applications," *Adv. Opt. Photonics*, vol. 9, no. 2, p. 257, Jun. 2017, doi: 10.1364/AOP.9.000257.



- 590 [43] V. Cremers, R. L. Puurunen, and J. Dendooven, "Conformality in atomic layer deposition: Current status
591 overview of analysis and modelling," *Appl. Phys. Rev.*, vol. 6, no. 2, p. 021302, Jun. 2019, doi:
592 10.1063/1.5060967.
- 593 [44] Jyoti *et al.*, "Recent advances in Metal-Organic Framework-Based fiber optic sensors and Photodetectors:
594 Synthesis, Properties, and applications," *Chem. Eng. J.*, vol. 507, p. 160543, Mar. 2025, doi:
595 10.1016/j.cej.2025.160543.
- 596 [45] X. J. Liang, A. Q. Liu, C. S. Lim, T. C. Ayi, and P. H. Yap, "Determining refractive index of single living cell
597 using an integrated microchip," *Sens. Actuators Phys.*, vol. 133, no. 2, pp. 349–354, Feb. 2007, doi:
598 10.1016/j.sna.2006.06.045.
- 599 [46] M. Schürmann, J. Scholze, P. Müller, J. Guck, and C. J. Chan, "Cell nuclei have lower refractive index and
600 mass density than cytoplasm," *J. Biophotonics*, vol. 9, no. 10, pp. 1068–1076, Oct. 2016, doi:
601 10.1002/jbio.201500273.
- 602 [47] A. Hossan, M. A. S. Chowdhury, S. T. Islam, and K. Z. Ferdwushee, "Design and optimization of an optical
603 ring resonator based biosensor for cancer detection," *Discov. Electron.*, vol. 2, no. 1, p. 50, Jun. 2025, doi:
604 10.1007/s44291-025-00090-x.
- 605
- 606



Data Availability Statement

The data supporting this study are available from the corresponding author upon reasonable request.

